Acta Materialia 106 (2016) 229–238

Contents lists available at ScienceDirect

Acta Materialia

journal homepage: www.elsevier.com/locate/actamat

Full length article

Combined atom probe tomography and density functional theory investigation of the Al off-stoichiometry of κ-carbides in an austenitic Fe–Mn–Al–C low density steel

M.J. Yao [a], P. Dey [a, *], J.-B. Seol [b, **], P. Choi [a], M. Herbig [a], R.K.W. Marceau [c], T. Hickel [a], J. Neugebauer [a], D. Raabe [a]

[a] Max-Planck-Institut für Eisenforschung, Max-Planck-Straße 1, 40237 Düsseldorf, Germany
[b] National Institute for Nanomaterials Technology, POSTECH, Pohang 790-784, South Korea
[c] Deakin University, Institute for Frontier Materials, Geelong, VIC 3216, Australia

ARTICLE INFO

Article history:
Received 6 October 2015
Received in revised form
19 December 2015
Accepted 5 January 2016
Available online xxx

Keywords:
Austenitic low density steel
Coherent precipitates
Off-stoichiometry
Atom probe tomography (APT)
Density functional theory (DFT)

ABSTRACT

We report on the investigation of the off-stoichiometry and site-occupancy of κ-carbide precipitates within an austenitic (γ), Fe-29.8Mn-7.7Al-1.3C (wt.%) alloy using a combination of atom probe tomography and density functional theory. The chemical composition of the κ-carbides as measured by atom probe tomography indicates depletion of both interstitial C and substitutional Al, in comparison to the ideal stoichiometric $L'1_2$ bulk perovskite. In this work we demonstrate that both these effects are coupled. The off-stoichiometric concentration of Al can, to a certain extent, be explained by strain caused by the κ/γ mismatch, which facilitates occupation of Al sites in κ-carbide by Mn atoms (Mn^{γ}_{Al} anti-site defects). The large anti-site concentrations observed by our experiments, however, can only be stabilized if there are C vacancies in the vicinity of the anti-site.

1. Introduction

There is a strong demand for the development of advanced high-strength steels for automotive applications, in order to reduce energy consumption and greenhouse gas emission. Austenitic Fe–Mn–Al–C steels show particularly outstanding mechanical properties [1–11] and are therefore highly promising candidates for such applications. Due to their good oxidation and corrosion resistance, these steels were originally developed in an attempt to substitute Cr-containing stainless steels [1], but recently they have regained interest due to their excellent strength-ductility balance and significantly reduced mass density due to alloying with Al [2–11].

A common characteristic of alloys showing excellent strength and ductility is a pronounced strain hardening capability, which continuously increases the strength and delays local necking during deformation. Transformation induced plasticity (TRIP) and twinning induced plasticity (TWIP) steels are typical examples for alloys showing high strain hardening capabilities [12,13], where martensitic transformation and formation of deformation twins are the respective dominant deformation and strain hardening mechanisms. The active deformation mechanisms are closely related to the stacking fault energy (SFE). Generally, as the SFE increases, the dominant deformation mechanism changes from TRIP to TWIP and from TWIP to dislocation gliding [14,15].

Gutierrez-Urrutia et al. attributed the excellent strain hardening capacity of solid solution austenitic Fe–Mn–Al–C alloys containing <5 wt.% Al to multiple stages of deformation during which sequential dislocation cell structures and, at higher loads, twin substructures are gradually formed [4]. For alloys of >5 wt.% Al, intragranular precipitation of nanometer-sized κ-carbides occurs at elevated temperatures (470 °C–710 °C) [16–19], which leads to a substantial increase in yield strength without a significant loss in ductility [3,5,8]. Planar dislocation substructures were observed in deformed κ-carbide containing austenitic Fe–Mn–Al–C alloys [5,6,10]. The occurrence of planar dislocation substructures in these alloys, which have high SFE values ranging from 80 to 110 mJ/m^2 [10], was ascribed to shearing of ordered κ-carbides by dislocations

* Corresponding author.
** Corresponding author.
E-mail addresses: p.dey@mpie.de (P. Dey), jb_seol@postech.ac.kr (J.-B. Seol).

http://dx.doi.org/10.1016/j.actamat.2016.01.007
1359-6454/

[6,8] and a mechanism referred to as "glide plane softening" [20]. According to this mechanism, the local order is destroyed by a leading dislocation shearing the ordered particle and thus facilitating the glide of consecutive trailing dislocations. For high strain levels, mechanisms of shear-band-induced plasticity (SIP) [2] and microband-induced plasticity (MBIP) [9,10] have been suggested, referring to homogeneous shear deformation and bands of very high dislocation density, respectively.

However, the interaction between dislocations and κ-carbide precipitates in age-hardened austenitic Fe–Mn–Al–C steels is still not well understood. Debates exist over the dominant co-deformation mechanism, i.e. the competition between dislocation looping [6] and precipitate shearing [8] during plastic deformation. It was reported that the critical size of ordered coherent precipitates for the transition from shearing to looping is associated with the antiphase boundary (APB) energy on the slip planes [21]. Therefore, an accurate determination of the stoichiometry and site-occupancy of κ-carbides is essential for understanding the strain hardening mechanisms in age-hardened austenitic Fe–Mn–Al–C alloys. Also, the exact sub-lattice occupancy in such a two-phase material containing ordered precipitates determines the elastic misfit across the hetero-interfaces. This will also contribute to the total system energy and to the strain hardening behavior.

The composition of κ-carbides is commonly given as $(Fe,Mn)_3AlC_x$, where the exact chemical composition of this phase is still unknown [17–19,22,23]. It is tacitly assumed to be a derivative from the Fe_3AlC_x-type ternary κ-carbide [24]. Due to the difficulty in determining C concentrations in small precipitates and also obtaining single-phase κ-carbide, the exact composition of the Fe_3AlC_x-type κ-carbide was uncertain for a long time [25,26]. In 1995, Palm et al. revealed a composition range for this phase between $Fe_{3.2}Al_{0.8}C_{0.71}$ and $Fe_{2.8}Al_{1.2}C_{0.42}$, i.e. $Fe_{3+y}Al_{1-y}C_x$ ($-0.2 < y < 0.2$, $0.42 < x < 0.71$), based on electron probe microanalysis (EPMA) [25]. The C content does not reach the stoichiometric 20 at.% and the Fe to Al ratio can vary between 2.3 and 4.0 instead of being equal to 3. Inspite of the fact that the deviation of the Fe to Al ratio is not appropriately considered in the common Fe_3AlC_x formula, it is still generally adopted. As for the $(Fe,Mn)_3AlC_x$ κ-carbide precipitates in Fe–Mn–Al–C alloys, since they are finely dispersed and only a few nanometers in size, their direct chemical characterization is challenging. Atom probe tomography (APT) is the ideal tool to resolve this composition uncertainty since it offers near-atomic spatial resolution and equal detection sensitivity to all elements [27–33]. To our knowledge, there are only two reports in the literature about APT analyses on κ-carbide-containing alloys. One is about κ-carbide precipitation in a ferritic matrix [34], with very different elemental partitioning behavior as compared to austenitic alloys. The second report deals with κ-carbide formation in austenitic Fe–Mn–Al–Si–Mo alloys [35], where Si is found to have a substantial effect on C partitioning. No APT data have been published on κ-carbide precipitates in quaternary austenitic Fe–Mn–Al–C alloys.

The crystal structure of κ-carbides is reported to be $L'1_2$ perovskite-type [17,22,36,37]. In such a derivative of the conventional face-centered cubic (fcc) crystal structure, the unit cell contains 5 atoms at 3 kinds of sites. In addition to the 4 atoms at one corner and three face-centered sites, as per fcc conventional unit cell, there is also one atom at the body-centered site. Conventionally, the elemental site-occupancy of the κ-carbide phase is such that Al occupies the corner site of the unit cell, Fe and Mn the face-centered positions, and C occupies the body-centered octahedral interstitial site, which is based on observations of electron diffraction patterns and calculations of structure factors [17,22,36]. In terms of atomic percentage, the stoichiometric $(Fe,Mn)_3AlC$ κ-carbide has 60% (Fe+Mn), 20% Al and remaining 20% C. However, the κ-carbides are commonly expected to be off-stoichiometric and thus the elemental site-occupancy remains unresolved. Since experimental characterization is challenging, a viable theoretical approach to elucidate the site-occupancy in κ-carbides is density functional theory (DFT).

In a separate work, the off-stoichiometry with respect to the depleted C concentration in κ-precipitates was interpreted with the aid of DFT simulations [38]. The off-stoichiometric C concentration was found to be driven by the minimization of the lattice misfit and hence the elastic strain between the coherent κ-precipitates and the γ-matrix. The current work is dedicated to the measurement of the chemical composition of κ-carbides at the atomic scale using APT followed by an interpretation of the experimental data on off-stoichiometry and site-occupancy in κ-carbide by means of DFT. The identified mechanisms are crucial for understanding the interaction between precipitates and dislocations during plastic deformation.

2. Methods

2.1. Alloy processing and APT measurements

The alloy of Fe-29.8Mn-7.7Al-1.3C (wt.%) (Fe-26.7Mn-14.1Al-5.3C (at.%)) as determined by wet chemical analysis was used in this study. It was prepared by vacuum-induction melting. The details of alloy casting and thermo-mechanical processing are reported elsewhere [5]. To obtain a homogenous microstructure, a solution heat treatment at 1100 °C for 2 h followed by water quenching was performed. Subsequently, the alloy was aged at 600 °C for 24 h to induce κ-precipitation. The grain size of the alloy ranged from ~50 to ~100 μm. The needle-like APT specimens, taken from grain interior regions, were prepared using a dual-beam focused-ion-beam (FIB) system (FEI Helios Nano-Lab 600*i*) by a standard FIB lift-out procedure, as described in Ref. [39]. Annular FIB milling was performed using a low acceleration voltage of 16 kV with final polishing at 2 kV to keep Ga^+ implantation into the samples at a negligible level. APT analyses were conducted using a LEAP 3000X HR system (Cameca Instruments) in voltage-pulsing mode at 200 kHz pulse repetition rate, 0.005 atom/pulse detection rate, 15% pulse fraction and 70 K. Six successful measurements were performed and evaluated, four of which contained more than 10 million ions. The APT data were evaluated using the IVAS software by Cameca Instruments (version 3.6.8), where the tip profile algorithm [40] was used for the reconstruction of APT maps.

2.2. Theoretical framework

The theoretical results were obtained using DFT [41,42] as implemented in the Vienna Ab Initio Simulation Package (VASP) [43]. Projector augmented wave (PAW) potentials were used to describe the electron–ion interaction [44] and the generalized-gradient approximation (GGA) functional of Perdew, Burke and Ernzerhof (PBE) [45] was employed. The single-electron wave functions were expanded using plane waves up to an energy cutoff of 500 eV. The Methfessel-Paxton method [46] was used for the Fermi surface smearing with a $6 \times 6 \times 6$ Monkhorst-Pack grid [47] for $2 \times 2 \times 2$ atomic supercells of both stoichiometric and off-stoichiometric κ-carbides. The energies converged to a precision of $\leq$1 meV/atom. Structural relaxations were performed until the forces on each atom were below 0.01 eV/Å. Cell shape and atomic positions were fully relaxed in all calculations, unless specified otherwise. The $2 \times 2 \times 2$ supercell of stoichiometric $(Fe,Mn)_3AlC$ κ-carbide is composed of 8 unit cells in $L'1_2$ structure with 5 sites/unit cell and occupied by 40 atoms ($(Fe_{16}Mn_8)Al_8C_8$). Here, Fe/Mn are situated at face-centered sites of each unit cell, Al at corner sites

and C atoms occupy the body-centered octahedral sites (Fig. 1(a)). An Fe to Mn ratio of 2:1 was employed based on the APT results. DFT studies reveal that configurational entropy is more favorable than chemical ordering in the face-centered Fe/Mn sub-lattice of κ-carbide above ~75 K [38]. The Fe/Mn chemical disorder was taken into account by a special quasi random structure (SQS) generation scheme [48] for the 2 × 2 × 2 supercell. It is important to note that all calculations were performed for ferromagnetic (FM) κ-carbide since the (Mn) anti-site formation energies computed for FM and paramagnetic states differed only by a small amount (~0.05 eV). Therefore, our DFT calculations [38] indicate that the consideration of paramagnetism, which is computationally much more demanding, does not qualitatively alter the results on structural properties and estimated point defect concentrations in κ-carbide.

3. Results

3.1. APT

3.1.1. Mass spectrum

Fig. 2 shows a representative mass spectrum of the studied austenitic alloy with κ-carbide precipitation. Peaks at 6, 6.5, 12, 13 Da are identified as carbon monomers. Apart from them, several peaks can be assigned to carbon molecular ions, similar to previous studies on other high-C containing alloys and carbides [49–54]. Peaks at 18, 18.5, 36 and 37 Da belong to carbon trimer ions. The carbon dimers $^{12}C_2^{1+}$ and $(^{13}C^{12}C)^{1+}$ are detected at 24 and 25 Da, respectively. The presence of 24.5 Da peak, which can be assigned to $(^{13}C^{12}C_3)^{2+}$, indicates the detection of carbon tetramers [51,52,55]. Hence, the peak at 24 Da does not only result from the carbon dimer $^{12}C_2^{1+}$ but also partly from $^{12}C_4^{2+}$. This overlapped peak can be decomposed by considering the peak at 24.5 Da $(^{13}C^{12}C_3)^{2+}$. According to the natural abundance of carbon isotopes ^{12}C and ^{13}C, the contribution of $^{12}C_4^{2+}$ to peak 24 Da can be estimated by its relative abundance ratio to $(^{13}C^{12}C_3)^{2+}$ [51,52,55]. The decomposition via the IVAS software indicates that $^{12}C_4^{2+}$ gives a contribution of about 37% to the peak at 24 Da. The $^{12}C_2^{2+}$ peak could in principle overlap with the $^{12}C^{1+}$ peak at 12 Da. However, the absence of a peak belonging to $(^{12}C^{13}C)^{2+}$ suggests that there is a negligible fraction of $^{12}C_2^{2+}$ at the peak at 12 Da.

Regarding substitutional elements, Fe^{2+} is detected at 27, 28, 28.5 and 29 Da and its primary isotope can also be detected at 56 Da ($^{56}Fe^{+}$) and 18.7 Da ($^{56}Fe^{3+}$). Mn^{2+} is detected at 27.5 Da. Peaks at 9 and 13.5 Da can be ascribed to Al^{3+} and Al^{2+}, respectively. Here it is also noted that according to the natural abundance of the isotopes of Fe, the peak at 27 Da cannot be completely assigned to $^{54}Fe^{2+}$. Al^{1+} ions must give a contribution to it as well [34,56]. The peak decomposition algorithm in IVAS indicates that 45% of this peak can be assigned to Al^{1+}. The measured total impurity concentration Si (14 Da) and Cr (26 Da) is less than 0.1 at.%. The material is a rather clean quaternary Fe–Mn–Al–C model alloy.

3.1.2. 3D morphology and arrangement of κ-carbides

Precipitation of coherent κ-carbides in the γ-matrix introduces an elastic stress field due to the lattice mismatch between precipitates and matrix [18]. The shape and arrangement of κ-precipitates are determined by the minimization of the sum of the elastic energy and the interfacial energy, arising from the κ/γ phase boundaries [57].

Fig. 3 shows the ordered $L'1_2$ –type κ-carbide precipitates within the austenitic (γ) matrix. The κ-carbides in the reconstructed 3D atom maps are visualized by 9 at.% C iso-concentration surfaces. APT reveals that cuboidal and plate-like κ-carbide particles are arranged in 3D in the form of stacks along three orthogonal directions which are identified by TEM observations as the elastically soft <001> crystallographic directions [5,6,18]. The spacing between two parallel stacks is on the order of 10–40 nm and will be referred to as broad γ channels. The spacing between individual precipitates within a stack is about 2–5 nm and will be referred to as narrow γ channels.

3.1.3. κ/γ elemental partitioning and phase compositions

Fig. 4(b) shows a 1D concentration profile along a particle stack through a cylindrical region of interest (ROI), which is highlighted in green in Fig. 4(a). Al and C atoms clearly partition to κ-carbides, whereas Mn exhibits only slight partitioning to γ. In order to closely compare the elemental partitioning into smaller plate-like and larger cuboidal κ-carbides, proximity histograms (proxigrams) [58] are employed to calculate the concentrations at fixed distances from their respective iso-concentration surfaces (9 at.% C). Fig. 4(c) depicts proxigrams from one large cuboidal κ-carbide κ_1^L and three small plate-like κ-carbides κ_1^S, κ_2^S and κ_3^S, which are highlighted in blue in Fig. 4(a). The proxigrams of the plate-like particles show slightly higher statistical errors due to smaller probed volumes as compared to the large cuboidal κ-carbide, but no compositional difference related to precipitate size and shape is observed. Fig. 4(b) and (c) reveal that the κ/γ interface has a thickness of ~2 nm, which could be larger than the actual value due to systematic measurement error and APT-related artifacts. Firstly, there is the local magnification effect as a result of different evaporation fields of two

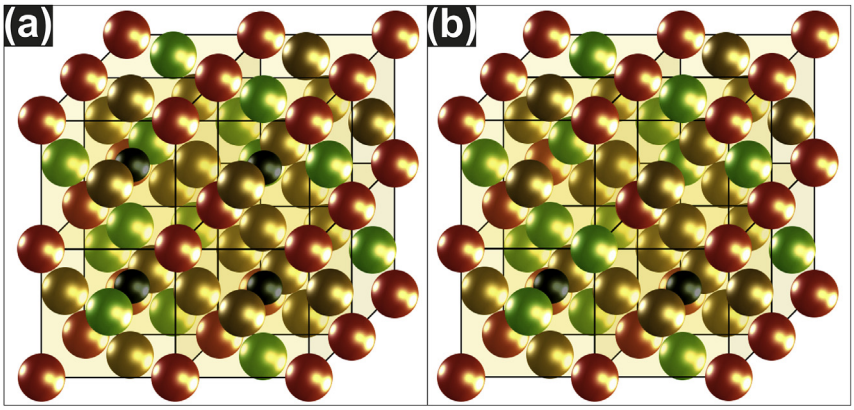

Fig. 1. Schematic visualization of the supercell of (a) stoichiometric $L'1_2$ κ-carbide, $(Fe_{16}Mn_8)Al_8C_8$, and (b) off-stoichiometric κ-carbide with a Mn anti-site at the Al sub-lattice and C vacancies, $(Fe_{16}Mn_8)(Mn_1Al_7)(C_5Vac_3)$, with chemical disorder in the Fe/Mn sub-lattice with an Fe:Mn ratio of 2:1. Fe, Mn, Al and C atoms are shown by golden, green, red and black balls, respectively. (For interpretation of the references to colour in this figure legend, the reader is referred to the web version of this article.)

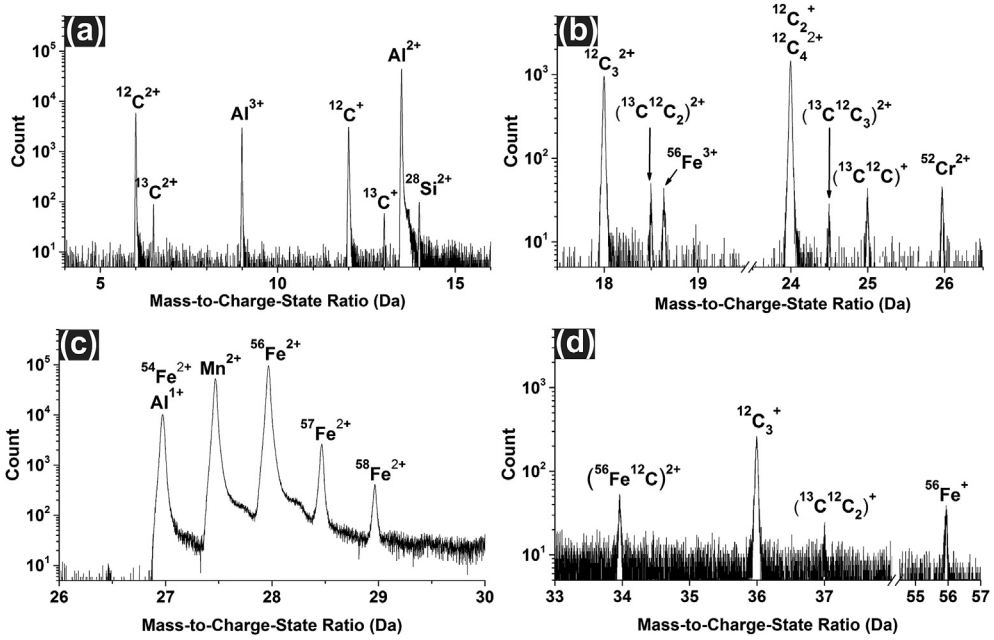

Fig. 2. APT mass spectrum of κ-carbide containing austenitic alloy: (a) 5–15 Da, (b) 18–26 Da, (c) 26–30 Da, (d) 33–57 Da. Ranges of mass-to-charge-state ratios without peaks are omitted. Peaks with ion overlap are marked with constituent ions.

phases, especially for interfaces parallel to the analysis direction [27,59]. If trajectories of neighboring surface atoms cross each other during field evaporation the reconstructed x-y positions of such ions are biased with an error and the apparent interface width in APT datasets is increased. Secondly, compositional signals can be smeared out due to data sampling. Since the detected κ/γ interfaces are not perfectly flat and exhibit some roughness and curvature, concentration gradients in 1D profiles become broadened even if the ROI is placed perpendicular to the interfaces. The finite sampling bin width (0.3 nm) leads to averaging of compositions of both abutting phases, increasing the apparent interface width. As for the proxigrams, the calculated distance of an atom to the nearest iso-surface is to a certain extent smeared out depending on voxel size and delocalization values.

When evaluating phase compositions, contributions from overlapping mass-to-charge peaks must be considered, which are however not taken into account in the above-shown concentration profiles and proxigrams. For a more accurate composition analysis decomposition of overlapping mass-to-charge peaks has to be performed. Hence, phase compositions were determined by clipping out the phases in the 3D atom maps by iso-concentration surfaces and subsequently analyzing their individual mass spectra by decomposition of overlapping mass peaks (C_2^+/C_4^{2+} and Al^+/Fe^{2+}). Threshold values for iso-concentration surfaces that isolate the κ-carbides and γ-matrix were chosen as ≥10 at.% C and ≤7 at.% C, respectively. These values correspond to the respective plateau C concentrations in κ and γ in the 1D concentration profiles and exclude the interfacial region from the analyses (Fig. 4(b)). Since no compositional difference was found between κ-carbide particles of different size and shape, an average composition value from all κ-carbides in the analyzed volume was determined.

The compositions determined, as listed in Table 1, reveal the same partitioning trend as that obtained from the proxigram analysis: κ-carbides are enriched with Al and C but depleted in Mn. The elemental partitioning between κ and γ can be quantified in terms of the corresponding partitioning coefficients $\varepsilon^i = c^i_\kappa/c^i_\gamma$, where c^i_κ and c^i_γ are the concentrations of element i (at.%) in the κ and γ phase, respectively. The values of the elemental partitioning coefficients ε are 0.92, 1.23 and 3.07 for Mn, Al and C, respectively.

3.2. DFT-based investigations of off-stoichiometry and site-occupancy

As stated before, if the κ-carbide had ideal stoichiometry, i.e. $(Fe,Mn)_3AlC$, its composition should be 60% (Fe+Mn), 20% Al and 20% C (at.%). However, the measured composition deviates from these values (Table 2). At first glance, there is an excess of Fe and Mn and a lack of C whereas the value for Al is close to the ideal value. The depleted C content indicates that the body-centered octahedral sites are not completely occupied by C atoms, but are either left vacant or occupied by metal atoms, e.g. the excess Fe or Mn atoms. In the following, we will therefore evaluate within DFT the probability of exchange mechanisms that could explain deviations from the ideal $L'1_2$ structure.

3.2.1. Metal and C sub-lattices interchange

We first compute the energy of Mn-free $Fe_{24}Al_8C_8$ κ-carbide with an interchange of a metal atom (Fe/Al) and an interstitial atom (C) and find it to be approximately 11 eV higher than the κ-carbide without such an interchange. We also investigate the scenario that Al (or Fe) from the matrix occupies the interstitial C site yielding a κ-carbide with $Fe_{24}Al_8(Al_1C_7)$ or that C from the matrix occupies a Fe (or Al) metal site yielding $Fe_{24}(Al_7C_1)C_8$. All these cases are energetically unfavored, which in turn indicates that metal atoms stick to substitutional sites, i.e. face-centered and corner sites, and C vacancies exist.

3.2.2. Al vacancies and $Fe^{\gamma}_{Al}/Mn^{\gamma}_{Al}$ anti-sites

The ratio of the Fe/Mn content (sharing the same face-centered sub-lattice) to the Al content (corner sub-lattice) is experimentally observed to be 3.4:1, instead of the stoichiometric 3:1, thereby indicating an excess of Fe and Mn and/or a depletion of Al. The underlying reason could be: (i) the presence of Al vacancies instead of a full occupation of this sub-lattice, or (ii) excess Fe or Mn atoms

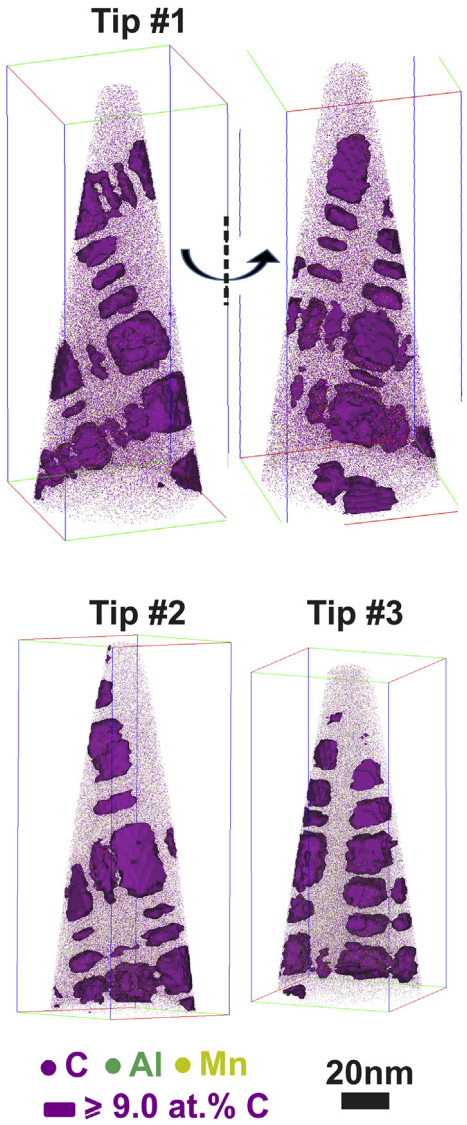

Fig. 3. Morphology and arrangement of κ-carbide precipitates: three representative reconstructed APT maps of C (purple), Al (green) and Mn (yellow) atoms. The κ-carbide precipitates are visualized with a 9 at.% C iso-concentration surface. (For interpretation of the references to colour in this figure legend, the reader is referred to the web version of this article.)

occupying the Al sub-lattice, i.e., the formation of anti-site defects. Since the experiments anticipate rather large defect concentrations in the order of 10% (discussed explicitly in section 4.1), we use the Fermi distribution

$$c = 1/\left[1 + \exp\left(E_f/k_B T\right)\right], \tag{1}$$

rather than the Boltzmann distribution [60] to account for the defect configurational entropy at finite temperatures. Here, E_f is the 0 K formation energy as obtained from DFT, T is the temperature and k_B the Boltzmann constant. The Fermi distribution prevents that two or more defects are placed at the same lattice site.

In order to consider off-stoichiometric configurations for Al, the impact of Al vacancies in the κ-carbide is investigated by calculating the formation energy of a vacancy at the Al site using the expression

$$E_f(Vac_{Al}) = E\left[(Fe_{16}Mn_8)(Al_7Vac_1)C_8\right] + \left(\mu_{Al} + \mu^0_{Al}\right) - E[(Fe_{16}Mn_8)Al_8C_8].\infty \tag{2}$$

Assuming thermodynamic equilibrium between the carbide and the surrounding matrix, the chemical potential μ_{Al} is determined by the composition of the matrix material (Table 1), whereas μ^0_{Al} is the T = 0 K reference energy (see Appendix for details). E $[(Fe_{16}Mn_8)(Al_7Vac_1)C_8]$ and E $[(Fe_{16}Mn_8)Al_8C_8]$ are bulk energies of κ-carbide with and without a vacancy, respectively.

Our calculations show that the vacancy formation energy can be as large as 2.62 eV, if an unstrained κ-carbide is assumed, yielding a diminishingly low Al vacancy concentration (~10^{-16}) at the aging temperature of 600 °C. The Al vacancy formation energy decreases to ~2.47 eV under consideration of hydrostatic strain induced by the coherency between the matrix and precipitate, which does not significantly alter the Al vacancy concentration. Interestingly, the strain dependence is much more severe in the case of C vacancies as shown in Ref. [38]. In fact, the experimentally observed C off-stoichiometry is a direct consequence of the reduction of inherent elastic strain in the coherent κ/γ system. The crucial role of elastic strain in pushing away C from κ-carbide was further manifested by the lower C concentration in coherently strained grain interior (GI) κ-carbides than the incoherent grain boundary (GB) κ-carbides.[1] However, for the formation of Al vacancies, the elastic strain field is found to have a negligible effect which is consistent with the chemical composition measured by APT [38]. While there exists a noticeable difference in the C concentrations in GI and GB κ-carbides, the difference in Al concentration is smaller. It can be thus concluded that the formation of Al vacancies in κ-carbides at 600 °C is not energetically favorable and fails to explain the off-stoichiometric Al concentrations in κ-carbides, which also indicates that the substitutional sites are completely occupied by metal atoms.

The next possible scenario considered to explain the Al depletion in the κ-carbides is the presence of Fe or Mn anti-site atoms at the Al sub-lattice. Considering the trend observed by APT that during precipitation Al partitions into κ-carbides while Fe and Mn out of them (Fig. 4(c), Table 1), this is a consequence of an incomplete de-mixing of the metal atoms on the fcc sub-lattices during precipitate formation. The point defect would still obey stoichiometry, if at the same time an Al anti-site on the Fe/Mn sub-lattice is formed. Our calculations reveal, however, that the formation of such stoichiometry conserving defect pairs is energetically not favored, because the Al anti-site has a high formation energy of more than 1 eV. The incomplete de-mixing must therefore be explained assuming a thermal equilibrium with the surrounding matrix material, as captured by the following expressions for the formation energies of such Mn^{γ}_{Al} or Fe^{γ}_{Al} anti-sites:

$$E_f(Mn^{\gamma}_{Al}) = E\left[(Fe_{16}Mn_8)(Mn_1Al_7)C_8\right] - \left(E\left[(Fe_{16}Mn_8)Al_8C_8\right] + \left(\mu_{Mn} + \mu^0_{Mn}\right) - \left(\mu_{Al} + \mu^0_{Al}\right)\right), \tag{3}$$

$$E_f(Fe^{\gamma}_{Al}) = E\left[(Fe_{16}Mn_8)(Fe_1Al_7)C_8\right] - \left(E\left[(Fe_{16}Mn_8)Al_8C_8\right] + \left(\mu_{Fe} + \mu^0_{Fe}\right) - \left(\mu_{Al} + \mu^0_{Al}\right)\right). \tag{4}$$

[1] GB κ-carbides start to precipitate after prolonged 600 °C-aging in this alloy system, as revealed in Ref. [38] and will be further studied elsewhere. They are negligible at the 24 h-aged state. In the current work, we concentrate on the off-stoichiometry of GI κ-carbides.

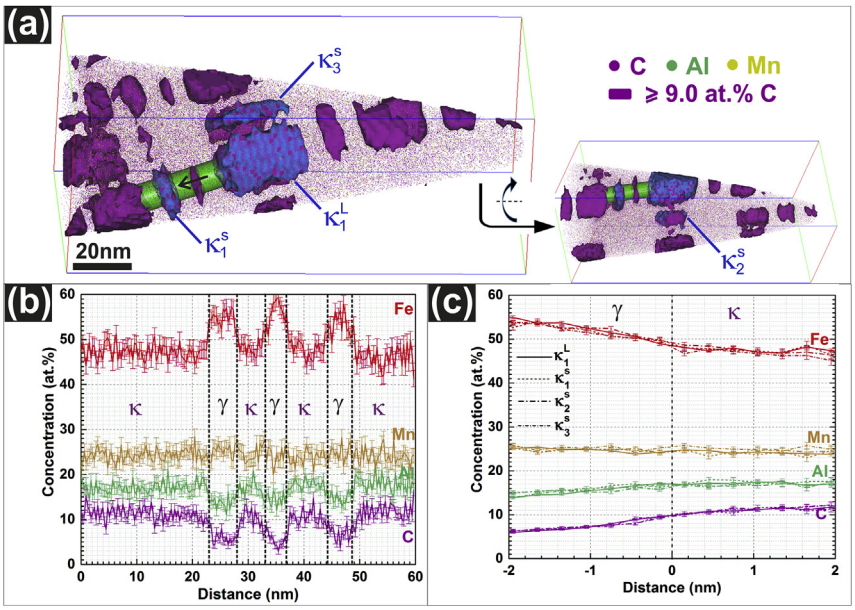

Fig. 4. (a) Reconstructed APT maps of C (purple), Al (green) and Mn (yellow) atoms. κ-carbide precipitates are visualized by a 9 at.% C iso-concentration surface; (b) 1D concentration profile of elements along the green cylinder (Φ = 10 nm) in (a) with a bin size of 0.3 nm. (c) Proxigrams with respect to interfaces between γ-matrix and κ-carbides highlighted in blue in (a), calculated with a bin size of 0.3 nm. (For interpretation of the references to colour in this figure legend, the reader is referred to the web version of this article.)

Table 1
Chemical compositions (at.%) of κ-carbides c_κ and γ-matrix c_γ determined by APT. Error bars indicate compositional fluctuations among different APT runs, while the statistical errors are negligible.

	Fe	Mn	Al	C
c_κ	43.4 ± 0.3	23.7 ± 0.3	19.8 ± 0.2	13.2 ± 0.4
c_γ	53.8 ± 0.2	25.8 ± 0.3	16.1 ± 0.1	4.3 ± 0.2

Here, $E[(Fe_{16}Mn_8)(Mn_1Al_7)C_8]$ and $E[(Fe_{16}Mn_8)(Fe_1Al_7)C_8]$ are the bulk energies of a κ-carbide with a Mn or Fe anti-site atom at the Al sub-lattice. As before, μ_X (X = Mn, Al or Fe) is the chemical potential of element X in the surrounding γ matrix and μ_X^0 are the T = 0 K reference potentials. The anti-site formation energies are computed as a function of lattice constant in order to elucidate the impact of strain induced by the surrounding γ matrix on anti-site formation (yellow shaded region in Fig. 5). Comparing the results for the pure anti-sites (squared symbols in Fig. 5), we observe that the Fe anti-site formation energies are substantially higher than for Mn and will be therefore excluded in the subsequent analysis to understand the Al off-stoichiometry.

The formation energies can then be used to calculate the equilibrium concentrations of Mn and Fe anti-sites using equation (1). However, the resulting concentration of Mn anti-sites at the equilibrium lattice constant (approx. 3.78 Å) in the absence of C vacancies is low (~10^{-5}) and undergoes only a negligible increase (to 10^{-4}) under volumetric compression (to 3.6 Å, the lattice constant of the γ matrix). These values are still much lower than the Al depletion measured by APT (~10^{-1}), which is discussed in detail later in Section 4.1. Hence, a strain effect alone is unable to explain the Al depletion within the κ-carbides.

3.2.3. *Combined C depletion and elastic strain effect on Mn^{γ}_{Al} anti-sites*

The experimental determination of κ-carbide composition suggests that not only Al but also C is depleted. The experimental composition (Table 2) has a C concentration of 13.2 at.%, i.e. lower than the stoichiometric 20 at.% C. Therefore, we next investigate the combined effect of C vacancies and elastic strain on the Mn anti-site formation in a supercell $(Fe_{16}Mn_8)(Mn_1Al_7)(C_{8-z}\ Vac_z)$, where the 40 sites contain z vacant body-centered interstitial sites (C vacancies) and an excess Mn atom on a Al-site as compared to the ideal $(Fe_{16}Mn_8)Al_8C_8$ with all sites (40) being completely occupied. Choosing only z = 3, which would be closest to the experimental

Table 2
The elemental site-occupancy of off-stoichiometric κ-carbide precipitate based on APT analysis in comparison to its ideal stoichiometry.

Chemical formula		Ideal stoichiometry	Off-stoichiometry
		$(Fe,Mn)_3AlC$	$(Fe_{2.00}Mn_{1.0})(Mn_{0.09}Al_{0.91})(C_{0.61}Vac_{0.39})$
Composition (at.%)	Fe	60	43.4
	Mn		23.7
	Al	20	19.8
	C	20	13.2
Occupation of all substitutional sites (%)	Fe	75	49.9
	Mn		27.3
	Al	25	22.8
Al depletion on its substitutional sub-lattice (%)		0	8.8
Occupation of body-centered interstitial sub-lattice by C (%)		100	60.8
C depletion on the body-centered interstitial sub-lattice (%)		0	39.2

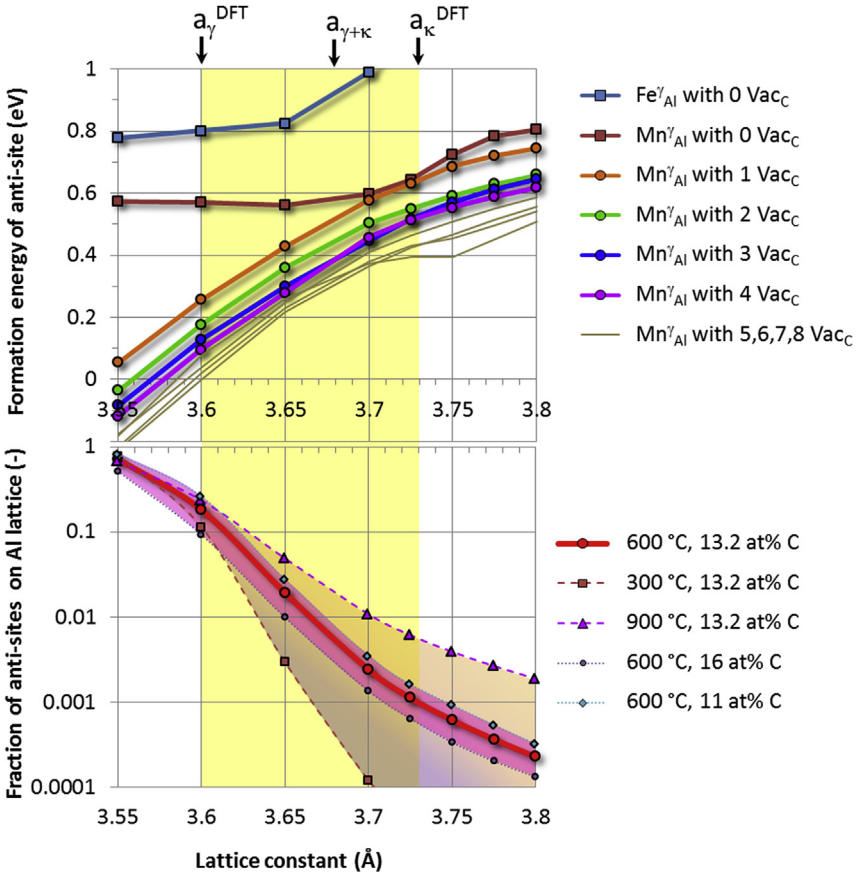

Fig. 5. Formation energies and concentrations of Fe$^\gamma_{Al}$ and Mn$^\gamma_{Al}$ anti-sites as a function of lattice constant for different C environments. The squared symbols in the upper panel mark the pure anti-site, whereas the circles mark complexes of anti-sites with a certain number of adjacent C vacancies, Vac$_C$. In the lower panel a sensitivity analysis for the dependence of Mn anti-site concentration for different equilibrium temperatures and total C concentrations in the carbide is performed. The possible change of the κ lattice constant (with composition $(Fe_{2.0}Mn_{1.0})(Mn_{0.125}Al_{0.875})(C_{0.625}Vac_{0.375})$) due to coherency strain to the γ matrix is highlighted by the yellow shaded region, where $a_{\kappa+\gamma}$ indicates the situation for an equal volume fraction of both phases. (For interpretation of the references to colour in this figure legend, the reader is referred to the web version of this article.)

composition, would correspond to a highly ordered vacancy distribution. Since the C vacancy interaction energies are too small (approx. 0.1 eV) to stabilize ordering effects at the annealing temperature 600 °C, we assume a random distribution of the C vacancies. The probability P(z) of z vacancies on the C sub-lattice adjacent to the considered anti-site, i.e., in the second nearest neighbor position, can be calculated using the following expression,

$$P(z) = N!/(z!(N-z)!)(p)^z(1-p)^{(N-z)} \quad (5)$$

where N is the total number of adjacent sites on the C sub-lattice (i.e., N = 8) and p is the probability that a particular site is vacant (i.e., p = 0.392, see Table 2). Using this combinatorial approach, not only three (P = 28%), but also one (P = 10%), two (P = 22%) and four (P = 23%) second neighbor vacancies have a high probability to occur in a sample with the given composition.

We clearly observe in Fig. 5 that the presence of C vacancies next to the Mn$^\gamma_{Al}$ anti-site reduces the anti-site formation energy. While the stabilization of the anti-site increases with increasing number of adjacent C vacancies, the strongest effect is observed for the first vacancy (i.e. $(Fe_{16}Mn_8)(Mn_1Al_7)(C_7Vac_1)$, see also Sec. 4.3). The vacancy effect alone is, however, not sufficient to explain the experimental anti-site concentrations. Even configurations with no adjacent C atoms (i.e. z = N = 8) have at the equilibrium lattice constant a_κ^{DFT} still an anti-site formation energy of ~0.4 eV, which is too large to yield substantial anti-site concentrations. A remarkable result is the strong dependence of the anti-site formation energy on volumetric strain, as soon as C vacancies are present on adjacent sites (Fig. 5). Under large volumetric compression, e.g., if the κ volume fraction is too small and thus the lattice constant of the coherent composite is close to that of the γ phase, the κ-carbide even becomes unstable, as indicated by the negative formation energy of the anti-site.

Using the above approach, we can compute the anti-site concentration for a given temperature by superimposing all possible configurations of adjacent C atoms. The results are shown in the lower panel in Fig. 5 and show an increase by several orders of magnitude (from 10^{-4} to 10^{-1}) as the κ-carbide undergoes volumetric compression due to the lattice misfit with the surrounding γ-matrix. Depending on the degree of compression of κ-carbide to the lattice constant of the surrounding γ-matrix (3.6 Å), the corresponding anti-site concentration is in the order of 10^{-1} (see Sec. 4.3 for details).

4. Discussion

4.1. Off-stoichiometry and site-occupancy of κ-carbides

The DFT calculations have revealed that (a) metal atoms are unlikely to occupy interstitial C sites and vice versa (section 3.2.1); (b) there is a full occupation of substitutional sites since the formation of Al vacancies is not favored (section 3.2.2). Considering (a) and the APT-measured reduced C content (13.2 at.% as shown in Table 1) as compared to the ideal stoichiometry (20 at.%), the

existence of C vacancies is confirmed. Since the existence of vacancies scales the elemental composition differently, we transform the description in terms of atomic percentage (Table 1) into a chemical formula $Fe_aMn_bAl_cC_x$. Here a+b+c=4 is the number of substitutional metal sites in a unit cell of $L'1_2$ structure and $x \leq 1$ is the portion of body-centered interstitial sites occupied by C. The fitting of the measured composition into such a form gives $(Fe_{2.00}Mn_{1.09}Al_{0.91})(C_{0.61}Vac_{0.39})$, fulfilling the substitutional/body-centered interstitial site ratio of 4:1. As compared to the nominal $(Fe,Mn)_3AlC$ perovskite, there is not only C vacancies but also an Al depletion in conjunction with an excess of (Fe+Mn). As shown in Table 2, instead of occupying 25% of the substitutional sites (corner sites), Al atoms only occupy 22.8% of them. In other words, 8.8% of the corner sites are not occupied by Al. This is not apparent, if the overall Al concentration of almost 20 at.% is considered.

The calculations show that Mn atoms rather than Fe atoms can fill the corner sites unoccupied by Al, if there is a C vacancy in the nearest-neighbor configuration and if the carbide is under volumetric compressive strain (Fig. 5). If this is applied to the chemical formula, one obtains $(Fe_{2.00}Mn_{1.0})(Mn_{0.09}Al_{0.91})(C_{0.61}Vac_{0.39})$.

In terms of a 40 atom DFT supercell this composition is best represented by $(Fe_{16}Mn_8)(Mn_1Al_7)(C_5Vac_3)$ (Fig. 1(b)). The corresponding Mn^{γ}_{Al} anti-site concentration at the experimental temperature of 600 °C found by DFT calculations (Fig. 5) is ~0.1 in the strained regime, which fits well with the experimental value of 8.8% (Table 2). The experimentally observed Al depletion can therefore be explained by the combination of Mn^{γ}_{Al} anti-sites and C vacancies under compressive strain caused by the coherency of the κ-carbides.

4.2. Compositional accuracy of APT measurements

Chemical compositions as determined by APT can be significantly affected by measurement conditions [40,49,51,59]. The effects of measurement parameters, including pulse fraction, specimen temperature and detection rate, on the apparent compositions of this highly alloyed Fe–Mn–Al–C steel will be discussed in another publication [61]. It was found that specimen temperature has a significant effect on the number of multiple events, which cause pile-up effects at the detector. The latter can lead to the preferential loss of a selected species [49–51]. For steels, Fe, being the main alloying element, produces the highest number of such multiple hit events and is thus likely to encounter the most severe detection losses [49–51,61]. The best agreement with the nominal composition was achieved at 70 K in the studied temperature range from 30 to 70 K [61], which was thereby chosen in this work. Our finding is also in good agreement with some previous work on binary Fe–C and ternary Fe–Mn–C alloys [49,50], where the best agreement between APT results and nominal bulk composition is obtained at 80 K and 60 K, respectively. Further increases in base temperature can lead to preferential field evaporation of selected species between voltage pulses, also referred to as DC field evaporation [59]. A high pulse fraction is known to suppress DC field evaporation [40,59]. Here a pulse fraction of 15% was chosen as a compromise between improved sample yield, constant pulse fraction throughout the dataset and minimal underestimation of the Mn composition of ~0.5 at.% as compared to a pulse fraction of 20% [61]. The detection rate has a minor effect on the apparent composition [61] and a value of 0.5% was chosen as a compromise between acquisition rate and sample yield.

Another source of error for compositional measurements with APT are peak overlaps in the mass spectrum, i.e. C_2^+/C_4^{2+} at 24 Da and Al^+/Fe^{2+} at 27 Da in these studies (see Fig. 2). The compositions of κ-carbides and the γ-matrix are determined by individual mass spectrum analysis with peak decomposition. Due to multiple events, the $^{56}Fe^{2+}$ isotope with the highest abundance can suffer most from detection loss, as mentioned above, which also affects the peak decomposition of the 27 Da peak. The loss of Fe due to detector pile-up leads to an overestimated Al concentration after deconvolution of the Al^+/Fe^{2+} peak at 27 Da [61]. Since the overall Al concentration is overestimated, the actual Al depletion in κ-carbide may be underestimated. The detection loss of primary element Fe also results in a slight overestimation of solute C concentration even under optimized measurement conditions [49,61], which suggests a potential underestimation of C depletion in κ-carbide. Additionally, we note that the acquisition parameters were optimized on homogenized single phase (γ) samples, but the field evaporation behavior of ordered κ-carbides is expected to be different from that of the disordered γ-phase.

4.3. Underlying issues related to DFT

The amount of Al depletion derived from our ab initio approach is also affected by uncertainties, for which we have performed a sensitivity analysis. First, the calculations are based on the assumption of a thermal equilibrium that is determined by the experimentally employed annealing temperature of 600 °C. We estimate the impact of this assumption by considering in addition two other temperatures that are 300 K below and above the annealing temperature, respectively (Fig. 5, lower panel, color gradient). For these (rather extreme) choices, the anti-site concentration changes – depending on the strain state – by up to one order of magnitude. However, the qualitative picture remains unchanged.

Second, the derived Al depletion is based on the assumption that in the experimental samples the C vacancies are mesoscopically homogeneously, but locally randomly distributed. To estimate the impact of C fluctuations we therefore change the overall C concentration from the experimental value (13.2 at.%) to 11 at.% and 16 at.%, respectively (Fig. 5, lower panel, red shading). As can be seen this has only little impact (approx. factor 2) on the resulting anti-site concentration.

Consequently, as outlined in the result part, the predicted anti-site concentration mainly depends on the volumetric strain, which is a direct consequence of the coherency to the γ-matrix. We therefore look in more detail on this aspect. Depending on the volume fraction of both phases [38], the equilibrium value of lattice parameter of the carbide-matrix composite can vary between the lattice parameter of κ-carbide and that of the γ-matrix (Fig. 5, yellow shaded region). For the latter synchrotron radiation yielded 3.68 Å, slightly deviating from 3.6 Å as predicted by our DFT calculations. This discrepancy can be due to the approximation of the exchange-correlation functional in DFT. Further, our finite supercell size yields a small deviation between the experimental and theoretical composition (53.8Fe-25.8Mn-16.1Al-4.3C vs 54.5Fe-27.3Mn-15.2Al–3C, at.%, respectively), in particular a lower Al concentration that can result in different lattice constants. Another reason may be our assumption of an anti-ferromagnetic rather than a paramagnetic spin configuration (see Appendix). For consistency reason, we have used in Fig. 5 the DFT lattice constant of 3.6 Å for the lower boundary. Due to the above considerations, the lattice constant $a_{\kappa+\gamma}$ highlighted in Fig. 5 for the composite (determined by taking the elastic strain energy into account) can only serve as an estimate, indicating that anti-site concentrations of several percent are predicted by our ab-initio approach.

In order to understand the surprisingly strong dependence of the anti-site formation energy on the C vacancy content in the regime of large volumetric strain, we investigated the effect of strain on the binding energy between Al and C in pure γ-Fe. Our results show that this binding energy changes from repulsion to

attraction when going from the strain free to the maximum strained configuration. The negligible effect of large volumetric strain on the anti-site formation in the absence of C vacancies (Fig. 5) can, therefore, be explained such that the energy gain from the formation of Mn anti-site under strain is compensated by the stronger loss of Al–C binding energy. Once the first C vacancy is present, i.e. there are less C atoms than Al atoms in the system, the formation energy of Mn^{γ}_{Al} anti-site is significantly reduced (Fig. 5).

5. Conclusions

We have investigated the off-stoichiometry and site-occupancy of κ-carbides in austenitic Fe-29.8Mn-7.7Al-1.3C low density steels by combined APT and DFT. The chemical composition of the κ-carbides determined by APT was found to be off-stoichiometric. Compared to the expected stoichiometric bulk $L'1_2$ perovskite composition, sub-lattice depletion was detected not only for the interstitial C sites but also for the substitutional Al sites. DFT calculations were employed to understand the off-stoichiometry and predict the corresponding site-occupancy for the chemical compositions measured by APT. The formation of Al vacancies and the corresponding reduction of the elastic coherency strains, which was found in a previous study to cause the C depletion in κ-carbides [38], cannot explain the detected Al depletion in κ-carbides. Instead, the off-stoichiometry is a consequence of rather low formation energies for Mn^{γ}_{Al} anti-sites when assuming thermodynamic equilibrium of this defect with the surrounding matrix. Such Mn^{γ}_{Al} anti-sites are energetically favored under compressive elastic strain (as occurring in coherent κ-carbide precipitates) only if neighboring C vacancies are present.

Hence, based on this joint APT and DFT work we have successfully explained that the Al depletion of coherent κ-carbide in a γ-matrix is occurring concurrently with a reduced C content in the precipitate. This off-stoichiometry is expected to modify the strengthening effect by the precipitate due to reduction in APB energy and should therefore be taken into account in the further modeling of the plasticity mechanisms such as SIP or MBIP.

Acknowledgments

We acknowledge financial support by Deutsche Forschungsgemeinschaft (DFG) within the SFB761 “steel ab initio”. M.Y. acknowledges financial support by the European Research Council through the advanced grant ‘Smartmet’. R.K.W.M. acknowledges the support of the Alexander von Humboldt Foundation through the award of a Humboldt Postdoctoral Fellowship. The authors also thank I. Gutierrez-Urrutia for helpful discussions.

Appendix

Determination of chemical potentials in the matrix material

We compute the Al vacancy formation energy and anti-site formation energies from the chemical potentials determined by the composition of the matrix. The experimental composition of the γ-matrix as determined by atom probe tomography (Fe-25.8Mn-16.1Al-4.3C in at.%) is approximated within our theory by choosing a chemically disordered 2 × 2 × 2 supercell (SC) with a composition of $Fe_xMn_yAl_z$. Here, the special quasi random structure (SQS) scheme has been employed. We choose antiferromagnetic (AFM) ordering, which is found to be the magnetic ground state for the chemically disordered structures, instead of the PM state, which is more realistic at finite temperatures. This is based on our findings discussed in Ref. [38] which shows that magnetism has no significant impact on structural properties of κ-carbide and its off-stoichiometric C concentration as well as the assumption that similar arguments also hold for the γ-matrix.

The first step to obtain chemical potentials is to determine the formation energy of the alloy with a composition (without C) close to the experimental composition as given by

$$E_f = E^{\gamma}\left[Fe_xMn_yAl_z\right] - x\mu^0_{Fe} - y\mu^0_{Mn} - z\mu^0_{Al}. \tag{A.1}$$

Here, $E^{\gamma}[Fe_xMn_yAl_z]$ is the total energy obtained by full relaxation of the SC with x, y and z being total number of Fe, Mn and Al atoms. μ^0_X is the bulk total energy per atom of the element X (=Fe, Mn or Al) and serves as a reference in the following. We choose AFM fcc Fe, AFM fcc Mn and NM fcc Al in order to calculate the total energy of elemental crystals. In the next step, the desired chemical potentials μ_X of Fe, Mn and Al in the matrix are derived from a self-consistent set of equations. On one hand, the formation energy obtained using Eq. (A.1) can be related to the chemical potentials by

$$x\mu_{Fe} + y\mu_{Mn} + z\mu_{Al} = E_f, \quad \mu_X = \overline{\mu}_X - \mu^0_X \tag{A.2}$$

i.e. $x\overline{\mu}_{Fe} + y\overline{\mu}_{Mn} + z\overline{\mu}_{Al} = E^{\gamma}[Fe_xMn_yAl_z]$.

Note that the additionally defined potentials $\overline{\mu}_X$ depend on the specific choice of the pseudopotential in the ab initio calculations. Therefore, only the subtraction of the bulk energies (μ^0_X) from $\overline{\mu}_X$ makes μ_X a physical quantity that can be related to an experimental composition. On the other hand, the exchange of atoms can be expressed by these additional potentials. If, for example, one Fe atom in the SC is substituted by a Mn atom, this yields

$$E^{\gamma}\left[Fe_{x-1}Mn_{y+1}Al_z\right] = E^{\gamma}\left[Fe_xMn_yAl_z\right] - \overline{\mu}_{Fe} + \overline{\mu}_{Mn} \tag{A.3}$$

Similarly, the substitution of a Fe atom in SC by Al atom yields

$$E^{\gamma}\left[Fe_{x-1}Mn_yAl_{z+1}\right] = E^{\gamma}\left[Fe_xMn_yAl_z\right] - \overline{\mu}_{Fe} + \overline{\mu}_{Al} \tag{A.4}$$

In order to obtain the chemical potentials for the composition $Fe_{3.6}Mn_{1.8}AlC_{0.2}$, DFT calculations for the SQS cell $Fe_{18}Mn_9Al_5$, and the defect SC's $Fe_{17}Mn_{10}Al_5$ and $Fe_{17}Mn_9Al_6$ have been considered in Eqns. (A.2) – (A.4), respectively. Note that certain deviations in the values of chemical potentials are present depending upon the choice made in substitution of atoms in Eqns. (A.3) – (A.4), however, this leads to minor changes in the results obtained for vacancy and anti-site formation energies.

References

[1] S.K. Banerji, An austenitic stainless steel without nickel and chromium, Met. Prog. 113 (1978) 59–62.
[2] G. Frommeyer, U. Bruex, Microstructures and mechanical properties of high-strength Fe-Mn-Al-C light-weight TRIPLEX steels, Steel Res. Int. 77 (2006) 627–633.
[3] H. Springer, D. Raabe, Rapid alloy prototyping: compositional and thermo-mechanical high throughput bulk combinatorial design of structural materials based on the example of 30Mn–1.2C– xAl triplex steels, Acta Mater 60 (2012) 4950–4959.
[4] I. Gutierrez-Urrutia, D. Raabe, Multistage strain hardening through dislocation substructure and twinning in a high strength and ductile weight-reduced Fe–Mn–Al–C steel, Acta Mater 60 (2012) 5791–5802.
[5] I. Gutierrez-Urrutia, D. Raabe, Influence of Al content and precipitation state on the mechanical behavior of austenitic high-Mn low-density steels, Scr. Mater 68 (2013) 343–347.
[6] I. Gutierrez-Urrutia, D. Raabe, High strength and ductile low density austenitic FeMnAlC steels: simplex and alloys strengthened by nanoscale ordered carbides, Mater. Sci. Technol. 30 (2014) 1099–1104.
[7] D. Raabe, H. Springer, I. Gutierrez-Urrutia, F. Roters, M. Bausch, J.-B. Seol, M. Koyama, P.-P. Choi, K. Tsuzaki, Alloy design, combinatorial synthesis, and microstructure–property relations for low-density Fe-Mn-Al-C austenitic steels, JOM J. Min. Met. Mat. S. 66 (2014) 1845–1856.
[8] K. Choi, C.-H. Seo, H. Lee, S.K. Kim, J.H. Kwak, K.G. Chin, K.-T. Park, N.J. Kim, Effect of aging on the microstructure and deformation behavior of austenite base lightweight Fe–28Mn–9Al–0.8 C steel, Scr. Mater 63 (2010) 1028–1031.
[9] J.D. Yoo, S.W. Hwang, K.-T. Park, Origin of extended tensile ductility of a Fe-

28Mn-10Al-1C steel, Metall. Mater. Trans. A 40A (2009) 1520–1523.
[10] K.-T. Park, Tensile deformation of low-density Fe–Mn–Al–C austenitic steels at ambient temperature, Scr. Mater 68 (2013) 375–379.
[11] K.M. Chang, C.G. Chao, T.F. Liu, Excellent combination of strength and ductility in an Fe–9Al–28Mn–1.8 C alloy, Scr. Mater 63 (2010) 162–165.
[12] C. Herrera, D. Ponge, D. Raabe, Design of a novel Mn-based 1GPa duplex stainless TRIP steel with 60% ductility by a reduction of austenite stability, Acta Mater 59 (2011) 4653–4664.
[13] I. Gutierrez-Urrutia, D. Raabe, Dislocation and twin substructure evolution during strain hardening of an Fe–22wt.% Mn–0.6 wt.% C TWIP steel observed by electron channeling contrast imaging, Acta Mater 59 (2011) 6449–6462.
[14] S. Allain, J.-P. Chateau, O. Bouaziz, S. Migot, N. Guelton, Correlations between the calculated stacking fault energy and the plasticity mechanisms in Fe–Mn–C alloys, Mater. Sci. Eng. A 387-389 (2004) 158–162.
[15] D. Pierce, J. Jiménez, J. Bentley, D. Raabe, C. Oskay, J. Wittig, The influence of manganese content on the stacking fault and austenite/ε-martensite interfacial energies in Fe–Mn–(Al–Si) steels investigated by experiment and theory,, Acta Mater 68 (2014) 238–253.
[16] K. Sato, K. Tagawa, Y. Inoue, Spinodal decomposition and mechanical properties of an austenitic Fe-30wt.% Mn-9wt.% Al-0.9 wt.% C alloy, Mater. Sci. Eng. A 111 (1989) 45–50.
[17] S. Tjong, Electron microscope observations of phase decompositions in an austenitic Fe-8.7 Al-29.7 Mn-1.04 C alloy, Mater. Charact. 24 (1990) 275–292.
[18] W.K. Choo, J.H. Kim, J.C. Yoon, Microstructural change in austenitic Fe-30.0 wt % Mn-7.8 wt% Al-1.3 wt% C initiated by spinodal decomposition and its influence on mechanical properties, Acta Mater 45 (1997) 4877–4885.
[19] K. Sato, K. Tagawa, Y. Inoue, Modulated structure and magnetic properties of age-hardenable Fe-Mn-Al-C alloys, Metall. Trans. A 21 (1990) 5–11.
[20] V. Gerold, H.P. Karnthaler, On the Origin of Planar Slip in Fcc Alloys, Acta Metall. 37 (1989) 2177–2183.
[21] A.J. Ardell, J.C. Huang, Antiphase boundary energies and the transition from shearing to looping in alloys strengthened by ordered precipitates, Philos. Mag. Lett. 58 (1988) 189–197.
[22] S. Tjong, Stress corrosion cracking behaviour of the duplex Fe-10Al-29Mn-0.4 C alloy in 20% NaCl solution at 100 °C, J. Mater Sci. 21 (1986) 1166–1170.
[23] K. Sato, K. Tagawa, Y. Inoue, Age hardening of an Fe-30Mn-9Al-0.9 C alloy by spinodal decomposition, Scr. Metall. Mater. 22 (1988) 899–902.
[24] R. Oshima, C. Wayman, Fine structure in quenched Fe-Al-C steels, Metall. Trans. 3 (1972) 2163–2169.
[25] M. Palm, G. Inden, Experimental determination of phase equilibria in the Fe-Al-C system, Intermetallics 3 (1995) 443–454.
[26] W. Sanders, G. Sauthoff, Deformation behaviour of perovskite-type phases in the system Fe-Ni-Al-C. I: Strength and ductility of Ni_3AlC_x and Fe_3AlC_x alloys with various microstructures, Intermetallics 5 (1997) 361–375.
[27] M.K. Miller, R.G. Forbes, Atom-probe Tomography: the Local Electrode Atom Probe, Springer, New York, 2014.
[28] T.F. Kelly, T.T. Gribb, J.D. Olson, R.L. Martens, J.D. Shepard, S.A. Wiener, T.C. Kunicki, R.M. Ulfig, D.R. Lenz, E.M. Strennen, First data from a commercial local electrode atom probe (LEAP), Microsc. Microanal. 10 (2004) 373–383.
[29] M.K. Miller, Atom Probe Tomography: Analysis at the Atomic Level, Springer, New York, 2000.
[30] F. Vurpillot, G. Da Costa, A. Menand, D. Blavette, Structural analyses in three-dimensional atom probe: a Fourier transform approach, J. Microsc. 203 (2001) 295–302.
[31] B. Gault, M.P. Moody, F. de Geuser, G. Tsafnat, A. La Fontaine, L.T. Stephenson, D. Haley, S.P. Ringer, Advances in the calibration of atom probe tomographic reconstruction, J. Appl. Phys. 105 (2009) 034913.
[32] D. Blavette, E. Cadel, A. Fraczkiewicz, A. Menand, Three-dimensional atomic-scale imaging of impurity segregation to line defects, Science 286 (1999) 2317–2319.
[33] M.J. Duarte, J. Klemm, S. Klemm, K. Mayrhofer, M. Stratmann, S. Borodin, A. Romero, M. Madinehei, D. Crespo, J. Serrano, Element-resolved corrosion analysis of stainless-type glass-forming steels, Science 341 (2013) 372–376.
[34] J.-B. Seol, D. Raabe, P. Choi, H.-S. Park, J.-H. Kwak, C.-G. Park, Direct evidence for the formation of ordered carbides in a ferrite-based low-density Fe–Mn–Al–C alloy studied by transmission electron microscopy and atom probe tomography, Scr. Mater. 68 (2013) 348–353.
[35] L.N. Bartlett, D.C. Van Aken, J. Medvedeva, D. Isheim, N.I. Medvedeva, K. Song, An atom probe study of kappa carbide precipitation and the effect of silicon addition, Metall. Mater. Trans. A 45 (2014) 2421–2435.
[36] K.H. Han, J.C. Yoon, W.K. Choo, TEM evidence of modulated structure in Fe-Mn-Al-C austenitic alloys, Scr. Metall. Mater. 20 (1986) 33–36.
[37] W.K. Choo, K.H. Han, Phase constitution and lattice parameter relationships in rapidly solidified $(Fe_{0.65}Mn_{0.35})_{0.83}Al_{0.17-x}C$ and $Fe_3Al_{1-x}C$ pseudo-binary alloys, Metall. Trans. A 16 (1985) 5–10.
[38] P. Dey, R. Nazarov, B. Dutta, M.J. Yao, M. Herbig, M. Friák, T. Hickel, D. Raabe, J. Neugebauer, Ab Initio Explanation of Disorder and Off-stoichiometry in Fe-Mn-Al-C κ-carbides, 2016. Unpublished results.
[39] K. Thompson, D. Lawrence, D.J. Larson, J.D. Olson, T.F. Kelly, B. Gorman, In situ site-specific specimen preparation for atom probe tomography, Ultramicroscopy 107 (2007) 131–139.
[40] D.J. Larson, T.J. Prosa, R.M. Ulfig, Local Electrode Atom Probe Tomography, Springer, New York, 2013.
[41] P. Hohenberg, W. Kohn, Inhomogeneous electron gas, Phys. Rev. Lett. 136 (1964) B864.
[42] W. Kohn, L.J. Sham, Self-consistent equations including exchange and correlation effects, Phys. Rev. 140 (1965) A1133.
[43] G. Kresse, J. Hafner, Ab initio molecular dynamics for open-shell transition metals, Phys. Rev. B 48 (1993) 13115.
[44] P.E. Blöchl, Projector augmented-wave method, Phys. Rev. B 50 (1994) 17953.
[45] J.P. Perdew, K. Burke, M. Ernzerhof, Generalized gradient approximation made simple, Phys. Rev. Lett. 77 (1996) 3865.
[46] M. Methfessel, A. Paxton, High-precision sampling for Brillouin-zone integration in metals, Phys. Rev. B 40 (1989) 3616.
[47] H.J. Monkhorst, J.D. Pack, Special points for Brillouin-zone integrations, Phys. Rev. B 13 (1976) 5188.
[48] A. Zunger, S.-H. Wei, L. Ferreira, J.E. Bernard, Special quasirandom structures, Phys. Rev. Lett. 65 (1990) 353.
[49] G. Miyamoto, K. Shinbo, T. Furuhara, Quantitative measurement of carbon content in Fe–C binary alloys by atom probe tomography, Scr. Mater. 67 (2012) 999–1002.
[50] R.K.W. Marceau, P. Choi, D. Raabe, Understanding the detection of carbon in austenitic high-Mn steel using atom probe tomography, Ultramicroscopy 132 (2013) 239–247.
[51] J. Takahashi, K. Kawakami, Y. Kobayashi, Quantitative analysis of carbon content in cementite in steel by atom probe tomography, Ultramicroscopy 111 (2011) 1233–1238.
[52] Y. Li, P. Choi, C. Borchers, S. Westerkamp, S. Goto, D. Raabe, R. Kirchheim, Atomic-scale mechanisms of deformation-induced cementite decomposition in pearlite, Acta Mater. 59 (2011) 3965–3977.
[53] H. Kitaguchi, S. Lozano-Perez, M. Moody, Quantitative analysis of carbon in cementite using pulsed laser atom probe, Ultramicroscopy 147 (2014) 51–60.
[54] M. Thuvander, J. Weidow, J. Angseryd, L.K. Falk, F. Liu, M. Sonestedt, K. Stiller, H.-O. Andrén, Quantitative atom probe analysis of carbides, Ultramicroscopy 111 (2011) 604–608.
[55] W. Sha, L. Chang, G. Smith, L. Cheng, E. Mittemeijer, Some aspects of atom-probe analysis of Fe-C and Fe-N systems, Surf. Sci. 266 (1992) 416–423.
[56] J.-B. Seol, D. Raabe, P.-P. Choi, Y.-R. Im, C.-G. Park, Atomic scale effects of alloying, partitioning, solute drag and austempering on the mechanical properties of high-carbon bainitic–austenitic TRIP steels, Acta Mater 60 (2012) 6183–6199.
[57] M. Doi, Elasticity effects on the microstructure of alloys containing coherent precipitates, Prog. Mater. Sci. 40 (1996) 79–180.
[58] O.C. Hellman, J.A. Vandenbroucke, J. Rüsing, D. Isheim, D.N. Seidman, Analysis of three-dimensional atom-probe data by the proximity histogram, Microsc. Microanal. 6 (2000) 437–444.
[59] B. Gault, M.P. Moody, J.M. Cairney, S.P. Ringer, Atom Probe Microscopy, Springer, 2012.
[60] S.A. Centoni, B. Sadigh, G.H. Gilmer, T.J. Lenosky, T.D. de la Rubia, C.B. Musgrave, First-principles calculation of intrinsic defect formation volumes in silicon, Phys. Rev. B 72 (2005) 195206.
[61] M.J. Yao, P. Choi, M. Herbig, P. Pinard, D. Raabe, Atom Probe Analysis of Massively Alloyed Fe-Mn-Al-C Light-weight Steel, 2016. Unpublished results.